AGU PUBLICATIONS

JGR

Journal of Geophysical Research: Solid Earth

RESEARCH ARTICLE

10.1002/2013JB010733

Key Points:
- Many states in turbulent spherical Couette flow depending on Rossby number
- Transitions affect angular momentum transport and internal field generation
- Dynamo-like enhancement of applied external dipole by nonaxisymmetric waves

Correspondence to:
D. P. Lathrop,
lathrop@umd.edu

Citation:
Zimmerman, D. S., S. A. Triana, H.-C. Nataf, and D. P. Lathrop (2014), A turbulent, high magnetic Reynolds number experimental model of Earth's core, *J. Geophys. Res. Solid Earth*, *119*, doi:10.1002/2013JB010733.

Received 30 SEP 2013
Accepted 22 MAY 2014
Accepted article online 28 MAY 2014

A turbulent, high magnetic Reynolds number experimental model of Earth's core

Daniel S. Zimmerman[1], Santiago Andrés Triana[2], Henri-Claude Nataf[3,4,5], and Daniel P. Lathrop[6]

[1]Institute for Research in Electronics and Applied Physics, University of Maryland, College Park, Maryland, USA, [2]Institute of Astronomy, KU Leuven, Leuven, Belgium, [3]Université Grenoble Alpes, ISTerre, Grenoble, France, [4]CNRS, ISTerre, Grenoble, France, [5]IRD, ISTerre, Grenoble, France [6]Physics, Geology, IREAP, IPST, University of Maryland, College Park, Maryland, USA

Abstract We present new experimental results from the University of Maryland Three Meter Geodynamo experiment. We drive a fully turbulent flow in water and also in sodium at magnetic Reynolds number $Rm = \Delta\Omega(r_o - r_i)^2/\eta$, up to 715 (about half design maximum) in a spherical Couette apparatus geometrically similar to Earth's core. We have not yet observed a self-generating dynamo, but we study MHD effects with an externally applied axisymmetric magnetic field. We survey a broad range of Rossby number $-68 < Ro = \Delta\Omega/\Omega_o < 65$ in both purely hydrodynamic water experiments and sodium experiments with weak, nearly passive applied field. We characterize angular momentum transport and substantial generation of internal toroidal magnetic field (the Ω effect) as a function of Ro and find a rich dependence of both angular momentum transport and Ω effect on Ro. Internal azimuthal field generation peaks at $Ro = 6$ with a gain as high as 9 with weak applied field. At this Rossby number, we also perform experiments with significant Lorentz forces by increasing the applied magnetic field. We observe a reduction of the Ω effect, a large increase in angular momentum transport, and the onset of new dynamical states. The state we reach at maximum applied field shows substantial magnetic field gain in the axial dipole moment, enhancing the applied dipole moment. This intermittent dipole enhancement must come from nonaxisymmetric flow and seems to be a geodynamo-style feedback involving differential rotation and large-scale drifting waves.

1. Introduction

The Earth's main magnetic field arises from partially understood processes in the outer core. The magnetic dynamo is thought to be driven by convective flows in the liquid iron outer core. One obstacle to quantitative modeling and prediction is turbulence. Estimates of the hydrodynamic Reynolds number, a measure of nonlinearity in the flow, give $Re = UL/\nu \approx 10^8$, where U is the velocity scale inferred in the core, L the size of the core, and ν an estimate of a typical viscosity for the liquid iron in the outer core. In liquid metals, the magnetic diffusivity $\eta = 1/(\mu\sigma)$ is much higher than the viscosity, so that the magnetic Prandtl number $Pr_m = \nu/\eta$ is very low (10^{-5} in the case of liquid sodium). Hydromagnetic flows of interest in geophysical and astrophysical situations have high magnetic Reynolds number $Rm = UL/\eta$, and the low magnetic Prandtl number implies that Re must be many orders of magnitude higher than Rm.

Direct numerical simulation becomes unfeasible with current computational tools not much above $Re \sim 10^6$ and requires high performance computing above $Re \sim 10^5$. Experimental models are useful because they reach higher Reynolds number than any simulation and have significant levels of turbulence. However, diagnostic measurements of the flow are limited compared to numerical simulations.

The success of the Riga [*Gailitis et al.*, 2001, 2008] and Karlsruhe [*Stieglitz and Müller*, 2001] experiments demonstrated that self-excitation was possible in fluid dynamo experiments and that theoretical predictions for the dynamo onset of a well-organized flow were accurate. These pioneer experiments also opened the way to second generation experiments, which aimed at producing dynamo onset in highly turbulent flows. However, it was discovered that turbulent fluctuations tend to oppose the dynamo action predicted for the mean flow [*Lathrop et al.*, 2001; *Petrelis et al.*, 2003; *Spence et al.*, 2006; *Frick et al.*, 2010; *Rahbarnia et al.*, 2012]. Nevertheless, the von Kármán Sodium experiment achieved self-excited field generation when ferromagnetic impellers are used, yielding a rich collection of dynamo behaviors [*Monchaux et al.*, 2007; *Berhanu et al.*, 2007; *Monchaux et al.*, 2009; *Berhanu et al.*, 2010].

Earth's dynamo is peculiar because its magnetic energy, E_M, is perhaps 4 orders of magnitude larger than the kinetic energy, E_K, of the large-scale convective motions inferred from the secular variation of the magnetic field [e.g., *Holme*, 2007]. This feature ($E_M >> E_K$) is not yet reproduced in numerical simulations, and it is not clear how this arises.

In Earth's core, the time scale for rotation ($\tau_\Omega = 1$ day) is much shorter than the time scale of magnetic (Alfvén) waves ($\tau_A \simeq 5$ years), which have been recently discovered [*Gillet et al.*, 2010]. As a consequence, motions are expected to be quasi-geostrophic on short time scales, while shaped by the magnetic field on long time scales [*Jault*, 2008; *Gillet et al.*, 2011].

These two conditions, $E_M >> E_K$ and $\tau_A >> \tau_\Omega$, are difficult to reproduce in the laboratory, and little is known about the organization of turbulence in these conditions. This was the motivation behind the *DTS* experiment in Grenoble. DTS has the same geometry and is driven by differential rotation as in the 3 m experiment described here, but DTS's outer shell is only 42 cm in diameter, and its inner sphere is a copper shell enclosing a strong permanent magnet [*Cardin et al.*, 2002; *Nataf et al.*, 2008; *Brito et al.*, 2011]. The DTS group observed that turbulent fluctuations are substantially reduced by the combined action of the Coriolis and Lorentz forces [*Nataf and Gagnière*, 2008].

We have constructed a 3 m diameter sodium spherical Couette experiment aimed at understanding better the role that rotation, magnetic fields, and turbulent fluctuations play in liquid metal dynamos. We have attempted to match Earth's core geometry, achieve a high magnetic Reynolds number and realistic magnetic Prandtl number in this experiment, and achieve an unusually low Ekman number.

A major difference between our experiment and planetary flows is that we drive the flow in the rotating frame using differential boundary rotation characterized by a Rossby number $Ro = \Delta\Omega/\Omega_o$, with $\Delta\Omega = \Omega_i - \Omega_o$. The large *Ro* of experiments presented here is not typical of the extremely low *Ro* in Earth's core. However, the actual *Ro* in the flow is not quite so high as is implied by the boundary speeds used to define our dimensionless control parameters. We have not yet thoroughly characterized this as a function of *Ro*, but *Sisan* [2004] finds a tangential velocity of about 16% the inner sphere's tangential velocity at $Ro = \infty$, and *Zimmerman et al.* [2011] finds local mean velocities corresponding to at most 20% of the outer sphere tangential velocity at $Ro = 2.13$. Despite the apparently large size of *Ro*, *Re*, and *Rm*, we use external driving quantities to define the dimensionless parameters as is traditional in experimental fluid mechanics so that comparison with other work is straightforward.

Although the mechanical forcing we employ is significantly different than Earth's core convective forcing, the two types of driving share some important properties. Instabilities first appear on the cylinder tangent to the inner sphere and form a ring of narrow columns with their axis aligned with the rotation axis [e.g., *Busse*, 1970; *Cardin et al.*, 2002; *Wicht*, 2014]. In both cases, the width of the columns decreases as the ratio of viscous to Coriolis forces decreases. As the forcing increases, the instabilities invade the bulk of the fluid shell. In the case of mechanical driving, the instabilities appear in the Stewartson layer that forms around the spinning inner sphere when the Reynolds number of the differential rotation gets large enough, and the threshold has been determined by *Wicht* [2014] for our geometry. All the experiments we present here are in regimes where the Reynolds number is more than hundred times critical.

2. Experiment Description

2.1. Mechanical Details

The experiment, shown schematically in Figure 1, consists of two independently rotating nonmagnetic stainless steel shells. The outer sphere, Figure 1a, has an inner radius $r_o = 1.46$ m, and the inner sphere, Figure 1b, has a radius of $r_i = 0.51$ *m* for a radius ratio $\Gamma = r_i/r_o = 0.35$, dimensionally similar to Earth's core. The inner sphere is supported on a 17 cm diameter shaft. The gap between the shells holds 12,500 L of fluid. In this paper, we present some results where the working fluid is molten sodium metal at approximately 120°C and others where the gap is full of tap water at approximately 20°C.

The density and viscosity of both fluids is similar, so purely hydrodynamic flow of each liquid would be essentially the same, but the sodium can interact strongly with magnetic field because of its high electrical conductivity, $\sigma \simeq 1 \times 10^7$ S/m. Since the boundaries are both made of low-permittivity, low-conductivity stainless steel, and the inner sphere is gas filled, the boundaries are approximately electrically insulating. The outer shell is one electromagnetic skin depth thick at a few hundred Hertz, and the inner shell is a skin

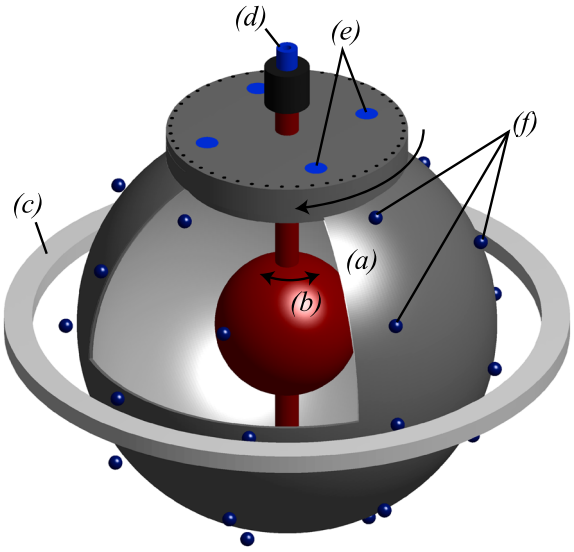

Figure 1. Schematic of the experiment. (a) Outer sphere (core-mantle-boundary), inner radius $r_o = 1.46 \pm 0.005$ m, 304SS stainless steel with thickness 2.5 cm and rotating at angular speed Ω_o. (b) Independently rotating (at Ω_i) inner sphere (inner core), hollow inert-gas-filled stainless steel, outer radius $r_i = 0.51 \pm 0.005$ m. The space between the two spherical boundaries (liquid outer core) is filled with 12,500 L of fluid, either water or sodium metal. (c) External magnet, B_0 at experiment center up to 160 G. (d) Torque transducer. (e) Instrumentation ports for fluid access, 60 cm from the rotation axis (pressure, wall shear stress and velocity in water, internal B_s and B_ϕ in sodium). (f) Hall sensor array (attached to and rotating with outer shell).

depth thick at several kHz. Both are therefore essentially transparent to the low-frequency magnetic fields induced by the sodium.

The boundaries are driven by a pair of 250 kW induction motors with variable frequency drives that hold the spheres' speeds constant to better than 0.2%. The inner sphere can be driven in either rotation direction with respect to the outer sphere, and the torque on the inner sphere is measured using a Futek TFF600 torque sensor and a 22 bit digitizer (Figure 1d). The outer sphere has been tested at the maximum design rotation rate of $\Omega_o/2\pi = 4$ Hz, and the design maximum speed of the inner sphere is approximately $\Omega_i/2\pi = 20$ Hz, but in the experiments described here, the maximum speeds we achieve are $\Omega_o/2\pi = 2.25$ Hz and $\Omega_i/2\pi = 9$ Hz.

Access to the flow in the rotating frame is provided through four 13 cm instrumentation ports shown in Figure 1e. These instrumentation ports are 60 cm away from the rotation axis and allow flush mounting of sensors on the outer sphere wall here. Wall pressure measurements in both sodium and water are made using Kistler 211B5 pressure transducers in three of these ports. In water experiments, ultrasound velocity measurements up to 30 cm from the outer sphere wall were conducted using a Met-Flow UVP-DUO and a home-made flush-mounted hot film system [see *Zimmerman*, 2010; *Zimmerman et al.*, 2011] was used to measure wall shear stress calibrated against torque measurements. In sodium experiments, a pair of Honeywell SS94A1F hall effect sensors are inserted into one instrumentation port to measure field in the azimuthal and cylindrical radial directions, and this will be discussed more in section 6.

2.2. External Field Configuration

We have not achieved self-excited dynamo action in sodium experiments. However, we will present some novel results regarding the interaction of the flow of sodium with an external axisymmetric magnetic field. In the experiments we report here, this field is applied by an electromagnet in the spheres' equatorial plane, Figure 1c. This magnet consists of 160 turns of square 1.3 cm aluminum wire with a cooling bore. The turns are arranged with a rectangular cross section 10 layers high and 16 layers radially with an inner magnet radius of 1.8 m and an outer magnet radius of 2 m.

We define our reference magnetic field B_0 as the magnitude of the applied field calculated at the exact center of the experiment:

$$B_0 = |\vec{B}_0(r = 0)|. \tag{1}$$

By varying the magnet's current from 0 to 300 A, B_0 can be varied from 0 up to a maximum of 160 G (16 mT). We normalize field quantities throughout the paper using calculated fields from the measured current instead of a measured field. There are two reasons for this. First, we do not have a magnetic measurement deep inside the experiment where the field is typical of the average strength inside the sodium. Second, we typically have substantial mean induction that would confound the use of a measurement to characterize the mean applied magnetic field. Our calculated value of B_0 agrees well with the measured field at all

sensor locations when the sodium is stationary or in solid body rotation, and the use of calculated values to nondimensionalize measured quantities allows easy interpretation of the mean induction.

The field from the single magnet in the equatorial plane varies appreciably throughout the experimental volume. It is roughly $2B_0$ at the equator and $B_0/2$ at the poles of the sphere. For the purposes of simulation the field from this magnet can be adequately modeled by the field of a single filamentary current loop with radius $r_\ell = 1.9$ m carrying 160 times the magnet current. This agrees to within a few percent of a finite element Biot-Savart calculation using a realistic multiturn geometry for our coil, and the deviations of that size are confined to a small region near the outer sphere equator.

2.3. Gauss Coefficients

An array of Honeywell SS94A1F Hall sensors in the rotating frame acquires time series of 31 measurements of the spherical radial component of the field, B_r, at a radius $r_p = 1.05r_o$. We build a model of the large-scale magnetic field outside the experiment by projecting these measurements onto vector spherical harmonics.

Outside the sphere where there are no currents, the only contributions to the total field are from poloidal vector spherical harmonics $\vec{S}_l^m$, which are given in spherical coordinates (r, θ, ϕ) by *Bullard and Gellman* [1954] as

$$\hat{r} \cdot \vec{S}_l^m(r,\theta,\phi) = l(l+1)\left(\frac{r_o}{r}\right)^2 f(r) Y_l^m(\theta,\phi) \tag{2}$$

$$\hat{\theta} \cdot \vec{S}_l^m(r,\theta,\phi) = \frac{r_o}{r}\frac{\partial f(r)}{\partial r}\frac{\partial Y_l^m(\theta,\phi)}{\partial \theta} \tag{3}$$

$$\hat{\phi} \cdot \vec{S}_l^m(r,\theta,\phi) = \frac{r_o}{r\sin\theta}\frac{\partial f(r)}{\partial r}\frac{\partial Y_l^m(\theta,\phi)}{\partial \phi}. \tag{4}$$

The Y_l^m are scalar spherical harmonics, and $f(r)$ is an arbitrary radial function. Outside the sphere, where the external magnetic field can be derived from a single scalar potential, $f(r) = r^{-l}$.

A common convention in geomagnetism is to report the measured magnetic field in terms of the Gauss coefficients g_l^m that represent the strength of each individual spherical harmonic. We assume a model of the external field with vector spherical harmonic components up to degree and order 4. We use a least squares fit of the radial component of this external field model evaluated at the 31 sensors' positions to the measured sensor data to obtain time series of the Gauss coefficients g_l^m:

$$\hat{r} \cdot \vec{B}(r,\theta,\phi,t) = \sum_{l=1}^{l=4}\sum_{m=0}^{m=l} l(l+1)\left(\frac{r_o}{r}\right)^{l+2} P_l^m(\cos\theta)\left(g_l^{m,s}(t)\sin\phi + g_l^{m,c}(t)\cos\phi\right), \tag{5}$$

where the $P_l^m(\cos(\theta))$ are Schmidt seminormalized associated Legendre polynomials.

Because of the symmetry breaking of rotation, standing nonaxisymmetric patterns in the rotating frame are not possible without pinning or special fine tuning, and the sine (s) and cosine (c) nonaxisymmetric Gauss coefficients often oscillate 90° out of phase. When we refer simply to g_l^m with $m \neq 0$, it can be assumed that both sine and cosine components are present to give an azimuthally drifting pattern.

In section 7, we will report the quantity $B_l^m = l(l+1)g_l^m$ evaluated at the outer sphere's inner surface so that it is easy to interpret the size of the different contributions. The quantity $B_l^m = l(l+1)g_l^m$ is the peak field strength of the radial field pattern at the "core-mantle boundary," which can easily be compared to the strength of the reference applied field B_0.

The field created by the equatorial current loop (treated as a single loop of radius r_ℓ) can be decomposed into Gauss coefficients as well [*Jackson*, 1975]. At the position of our magnetometers (inside the loop), the field is of external origin. But since we only consider B_r measurements at a single radius r_p, we can consider the same Gauss coefficients as defined above to get analytic B_1^0 and B_3^0 coefficients of the applied field. We get

$$B_1^0 = \frac{\mu_0 N I}{2r_\ell} \tag{6}$$

and

$$B_3^0 = -3\left(\frac{r_p}{r_\ell}\right)^2 \frac{\mu_0 NI}{4r_\ell}, \tag{7}$$

where NI is the total ampere-turns of the loop ($160I_{\mathrm{mag}}$). With $r_p/r_\ell \simeq 0.8$, we find that the applied field contribution to the B_3^0 coefficient in our inversions is almost perfectly opposite to that of the B_1^0 coefficient.

3. Dimensionless Parameters

3.1. Flow Dimensionless Parameters

We define the fluid and magnetic Reynolds numbers Re and Rm with $\Delta\Omega = \Omega_{\mathrm{i}} - \Omega_{\mathrm{o}}$:

$$Re = \frac{\Delta\Omega(r_{\mathrm{o}} - r_{\mathrm{i}})^2}{\nu} \qquad Rm = \frac{\Delta\Omega(r_{\mathrm{o}} - r_{\mathrm{i}})^2}{\eta}. \tag{8}$$

The kinematic viscosity ν is approximately 1×10^{-6} m^2/s for water and 7×10^{-7} m^2/s for sodium. Actual values of density and viscosity used in calculations of dimensionless parameters are taken from *Lemmon et al.* [2013] for water and from *Fink and Leibowitz* [1995] for sodium. The magnetic diffusivity of sodium $\eta = (\sigma\mu_0)^{-1}$ is 0.079 m^2/s. We have verified this value in our experiment by applying an axisymmetric field to stationary liquid sodium, interrupting the current, and measuring the time constant for the exponential resistive decay of the axial dipole component $\tau_{\mathrm{dip}} = r_{\mathrm{o}}^2/(\pi^2\eta)$. The measured value of $\tau_{\mathrm{dip}} \simeq 2.7$ s is consistent with a calculation based on the value of conductivity reported in *Fink and Leibowitz* [1995].

We define the Ekman number, expressing the importance of viscous to Coriolis forces, using the outer sphere angular speed:

$$E = \frac{\nu}{\Omega_{\mathrm{o}}(r_{\mathrm{o}} - r_{\mathrm{i}})^2}. \tag{9}$$

Because of the large size, rapid rotation, and low viscosity, our Ekman number is among the lowest achieved in rotating fluid experiments to date. We express the dimensionless differential rotation as a Rossby number:

$$Ro = \frac{\Delta\Omega}{\Omega_{\mathrm{o}}}. \tag{10}$$

Here we have chosen a velocity scale $U = \Delta\Omega(r_{\mathrm{o}} - r_{\mathrm{i}})$ so that $Re = Ro/E$. As viewed from the laboratory frame, the inner sphere can superrotate ($Ro > 0$), subrotate ($-1 < Ro < 0$), or counterrotate ($Ro < -1$) with respect to the outer. As viewed from a frame rotating with the outer shell where we make most measurements, $Ro < 0$ is retrograde rotation of the inner sphere and $Ro > 0$ is prograde.

3.2. Turbulence and the Size of *Re*, *Ro*, and *Rm*

We define our experimental parameters *Re*, *Rm*, *Ro*, etc. based on boundary speeds instead of measured velocities (which are a response of the system to the boundary forcing) because this allows straightforward comparisons between different experiments and simulations. However, as we mention in section 1 the velocities driven in most of the volume in wide gap shear flows by the rapidly rotating boundaries are much lower than the boundary speeds. We generally expect turbulent flows at high *Re*, but we should address this given that measured velocities in the system are substantially lower and therefore imply lower *Re* and *Rm*. Several measurements and estimates can be used to show that while we do not achieve a system response *Re* near 10^8, we do not present results with *Re* lower than about 10^5, high enough that we may expect asymptotic behavior and some sort of turbulence.

Similarly *Rm* is substantially lower than implied by the boundary speeds, a serious issue for strong MHD effects, but an issue shared across the literature of boundary-driven spherical Couette MHD experiments.

A typical velocity characterizing a turbulent shear flow is the friction velocity $u^* = \sqrt{\tau/\rho}$, where τ is the wall shear stress and ρ is the fluid density. If we assume uniform wall shear stress on the inner sphere, then $\tau = T/(\pi^2 r_{\mathrm{i}}^3)$ where T is the torque (we do not use our wall shear stress sensor for these estimates because it is calibrated against measured torque using similar assumptions). Typical torque-derived friction velocities for the results here are roughly 0.1 to 1 m/s (with the lower values at low *Ro*) and provide a Reynolds number $Re^* = u^* L/\nu$ which ranges roughly from 90,000 to 900,000.

We expect rather inhomogeneous turbulence in a wide-gap boundary-driven system like this but require substantial Reynolds stresses from fluctuating velocities throughout a large volume of the fluid to explain

Table 1. Relevant MHD Parameters

Parameter	Definition	Section 7 Range[a,b]
Lundquist	$S = \frac{B_0(r_o - r_i)}{\eta\sqrt{\rho\mu_0}}$	$0 < S < 4.2$
Hartmann	$Ha = \frac{B_0(r_o - r_i)}{\sqrt{\rho\mu_0\eta\nu}}$	$0 < Ha < 1410$
Elsasser	$\Lambda = \frac{B_0^2}{\rho\mu_0\eta\Omega_o}$	$0 < \Lambda < 0.22$
Interaction Parameter	$N = \frac{Ha^2}{Re}$	$0 < N < 0.04$
Lehnert Number	$\lambda = \frac{B_0}{\Omega_o(r_o - r_i)\sqrt{\rho\mu_0}}$	$0 < \lambda < 0.056$

[a]"Zero" means $B_0 = 0$. Earth's field approximately 0.3% of maximum B_0.
[b]Largest possible values $S = 5.9$, $Ha = 1980$, $\Lambda = 14.4$, and $N = 8.7$.

the angular momentum transport we observe. Though we cannot provide a comprehensive study, there are a few previously published results in spherical Couette results for comparison.

Velocity measurements in *Zimmerman et al.* [2011] in the 3 m apparatus in water at $Ro = 2.13$ at an outer sphere rotation frequency of 0.75 Hz ($\Omega_o r_o = 7$ m/s) show velocity fluctuations near the outer sphere wall with RMS levels approximately 0.20 m/s and 0.30 m/s in the low and high torque states, respectively. Mean torque measurements on the inner sphere are 34 Nm and 50 Nm in these states, corresponding to u^* estimates of 0.17 and 0.20 m/s, which are comparable in magnitude to the fluctuations directly measured near the outer wall. The mean locally measured mean velocities near the outer sphere (dominated by the azimuthal velocity) are $\bar{u} = 0.52$ m/s in the high torque state (a local Rossby $Ro_L = \bar{u}/(\Omega_o r_o) = 0.076$) and $\bar{u} = 1.28$ m/s ($Ro_L = 0.186$) in the low torque state, both much lower than $Ro = 2.13$ defined using external boundary speeds, but sufficient to drive turbulent flow.

At $Ro = -0.6$, the direct numerical simulations of *Matsui et al.* [2011] report turbulent fluctuations throughout the fluid outside the tangent cylinder in a moderately magnetized state with strong excitation of an inertial mode. At this set of parameters, the mean flow in the rotating frame is localized inside the tangent cylinder and the maximum mean flow speed is of the order of the inner sphere tangential speed. And *Sisan* [2004] measures turbulent fluctuations on the order of 10%–20% of the mean flow at $Ro = \infty$ at a Reynolds number more than an order of magnitude lower than those reported here.

Finally, while they represent an indirect probe of turbulence, especially its strength, all magnetic and pressure spectra in our measurements here have substantial broadband fluctuations well above the noise floor at all parameters. Technical limitations have prevented a thorough direct characterization of the mean and fluctuating system response velocities at all *Ro* and *Re*, but the pieces of evidence we do have point to substantial turbulence. We do not mean to imply that there is uniform homogeneous turbulence, and indeed, we expect the turbulence to be strongly anisotropic, strongly inhomogeneous, and with a character that depends substantially on *Ro*.

3.3. Applied Field Dimensionless Parameters

The strength of the applied magnetic field in this paper will be expressed using the Lundquist number

$$S = \frac{B_0(r_o - r_i)}{\eta\sqrt{\rho\mu_0}} = \frac{V_{\text{Alfvén}}(r_o - r_i)}{\eta}, \tag{11}$$

in which $V_{\text{Alfvén}}$ is the typical velocity of Alfvén waves. The Lundquist number is a convenient dimensionless measurement of the magnetic field in the context of this paper. It is linear in the magnetic field and does not vary with *Ro*, *Re*, or *E*. Our strong field data in this paper are in a limited range of parameter space, so we do not have scaling of results that would suggest a better parameter for data collapse. However, for readers' reference and comparison with other works, Table 1 contains the definitions of other common MHD parameters and the ranges of those parameters accessed in the strong field results of section 7. For reference, we also list the extreme values of some parameters which can be achieved by the current machine configuration.

These extreme parameters allow us to access some novel dynamics. As we discussed in section 1, Earth's dynamo operates in a regime where the magnetic energy E_M is several orders of magnitude larger than the kinetic energy E_K. By applying a strong magnetic field, especially with weak forcing, we can examine this regime. It is interesting to explore turbulence where $E_M > E_K$ while *Rm* is still large enough to allow for strong induction effects.

We can estimate E_K assuming angular velocity profiles measured in hydrodynamic spherical Couette flow with the outer shell stationary [*Sisan*, 2004], obtaining $E_K \sim 0.02Rm^2$ in units of $\rho\eta^2(r_o - r_i)$. Integrating the

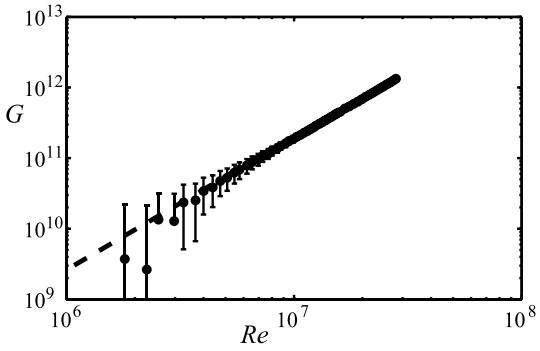

Figure 2. Dimensionless torque versus Reynolds number with outer sphere stationary ($Ro = \infty$) in water. The dashed line is a fit $G_\infty = 0.003Re^{1.89}$ [*Zimmerman*, 2010]. Error bars represent an estimate of the torque due to shaft seals, a substantial contribution to the total torque at low *Re*. An offset seal torque estimate measured with the experiment air filled is subtracted.

magnetic energy in the shell at maximum applied field gives $E_M = 150$ in the same units, meaning that $E_M > E_K$ up to nearly $Rm = 90$ (keeping in mind that the *effective* magnetic Reynolds number is lower as discussed in section 3.2). In contrast, *Nataf* [2013] reports that in the DTS experiment, $E_M > E_K$ only up to $Rm = 5$.

Furthermore, it is expected that short time scale dynamics are controlled by rotation in the Earth's core. *Jault* [2008] shows that this is the case when the Lehnert number

$$\lambda = \frac{B_0}{\Omega_o(r_o - r_i)\sqrt{\rho\mu_0}} \tag{12}$$

is less than 10^{-2}, that is, when Alfvén waves propagate 100 times more slowly than inertial waves. It is not difficult to achieve small λ in an experiment. However, the Lundquist number *S* must be high enough to allow Alfvén waves to propagate. In the DTS experiment, $S = 7.8$ near the inner sphere, but $\lambda \simeq 0.4$ at that location. In the 3 m experiment, the Lundquist number can be as high as 12 near the equator at just $\lambda = 0.04$ (here $S \simeq 6$, $\lambda \simeq 0.02$ at the center of the experiment).

We present some strong field results in section 7.

4. Torque Measurements

The torques on the boundaries of a rotating shear flow are interesting in the context of planetary fluid mechanics, since angular momentum is conserved in the fluid except by exchange with the rigid boundaries. Unlike a planet, we hold the rigid boundaries at fixed speed, maintaining a mean flux of angular momentum from one boundary to the other. However, the torque required to maintain fixed speeds is an interesting global measurement of this angular momentum flux and therefore of the angular momentum transport by the turbulent flow.

We note some similarities of our experiments with experimental results in Taylor-Couette flow. *Paoletti and Lathrop* [2011] and *van Gils et al.* [2011] established that the Rossby number (or similar dimensionless number related to the rotation rate ratio) has a strong effect on the angular momentum transport, with a torque peak at a certain value of Rossby in the counterrotating regime. We find a similar result with important quantitative similarities in spherical Couette flow over much of the measured range. We also observe differences for superrotation which lead to intermittent jumps in torque significantly exceeding typical RMS torque fluctuations due to large-scale flow transitions as in *Zimmerman et al.* [2011].

4.1. Reynolds Dependence at Fixed Rossby

We define a dimensionless torque *G*:

$$G = \frac{T}{\rho\nu^2 r_i}, \tag{13}$$

where *T* is the dimensional torque that the fluid exerts on the inner sphere. The torque at fixed Rossby number scales with an expected nearly quadratic Reynolds dependence as shown in Figure 2 with the outer sphere stationary ($Ro = \infty$). The experiment has rubber shaft seals that represent a substantial fraction of the measured torque at low *Re*. In Figure 2 we subtract a mean seal torque measured by running the experiment in air where the seal torque dominates. The seal torque subtracted from these measurements is constant with differential speed, contrary to the linear assumption used in *Zimmerman et al.* [2011] used prior to the air-filled measurements. Due to changes during rebuild between water and sodium experiments the seal torque for sodium experiments is 16.5 Nm and that for water is 11 Nm. The length of error bars in

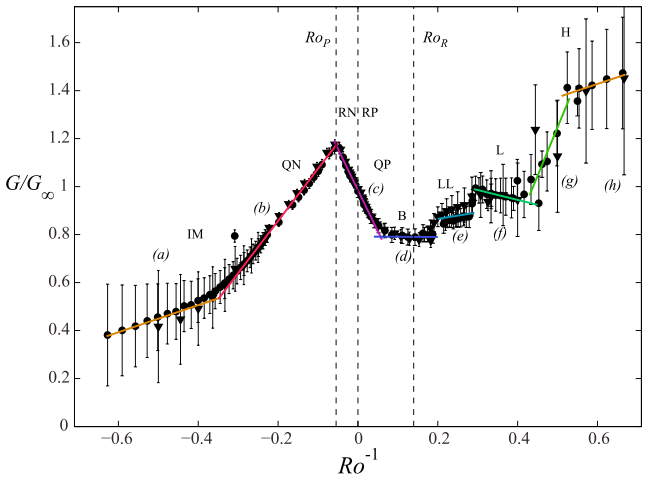

Figure 3. Rossby dependence of the magnitude of the measured inner sphere torque. The magnitude of the torque at a given *Ro* and *Re* is normalized by $G_\infty(Re)$, the torque expected at that Reynolds number if the outer sphere were stationary instead of rotating. A similar *Re* dependence of the torque at all *Ro* is also observed in Taylor-Couette flow [*Paoletti and Lathrop*, 2011; *van Gils et al.*, 2011]. The torque dependence on Ro^{-1} is fit well by a piecewise linear model. Fits to lines (a) through (h) are given in Table 2. We show both data from sodium experiments (black inverted triangle) and data from water experiments (black circle). The sodium data are taken with a weak applied external field, 20 A magnet current: $S = 0.39$ to measure magnetic induction. The vertical line Ro_P is the negative *Ro* peak of the torque defined by intersection of fit lines (b) and (c). At the "Rayleigh" line Ro_R, the inner and outer sphere equators have equal angular momenta.

Figures 2 and 3 is equal to the subtracted seal torque. Using a fit to data with outer sphere at rest, we define the quantity $G_\infty(Re)$:

$$G_\infty(Re) = 0.003Re^{1.89} \tag{14}$$

for all *Re* that we measure here. For comparison with equation (14), the implicit expression relating G_∞ and *Re* in Taylor-Couette flow, equation (2) of *Paoletti and Lathrop* [2011], can be approximated by $G_\infty(Re) = 0.03Re^{1.85}$ in the range of *G* in Figure 2. The prefactor of our G_∞ is much lower than that in Taylor-Couette flow, but this prefactor is a geometry-dependent friction factor that is likely to be much lower in the much wider gap of the 3 m experiment versus a Taylor-Couette experiment with much smaller radius ratio.

The total hydrodynamic torque as a function of Rossby and Reynolds, $G(Ro, Re)$, has a common *Re* dependence as explored in *Dubrulle et al.* [2005] and *Paoletti and Lathrop* [2011], and similarly here, we observe that the total torque, $G(Ro, Re)$, factorizes

$$G(Ro, Re) = f(Ro)G_\infty(Re). \tag{15}$$

We find that this is a common feature shared by turbulent Taylor-Couette and turbulent spherical Couette flow, but the form of $f(Ro) = G(Ro, Re)/G_\infty(Re)$ for spherical Couette flow is more complex, especially for $Ro > 0$. This will be discussed in the next two sections.

4.2. Rossby Dependence of Torque

The Rossby dependence of the torque in turbulent spherical Couette flow is shown in Figure 3. We measure the magnitude of the mean torque, $G(Ro, Re)$, in both water (black circle) and sodium (black inverted triangle) over a wide range of Rossby number. To measure induced field fluctuations and internal magnetic induction during the sodium runs, we applied a relatively weak magnetic field, 20 A magnet current for Lundquist $S = 0.39$. The close agreement between sodium and water torque dimensionless torque data suggests that there is not a significant dynamical effect of the Lorentz forces on the flow and inner sphere torque at this value of applied field, except perhaps in the region of fit line (e) (LL state) where the sodium and water data seem to depart systematically. As we will see in section 6, this region is a peak of the azimuthal magnetic induction with substantial gain and Lorentz forces from the total field might explain this departure.

Table 2. Empirical Fit Lines in Figure 3

Line	G/G_∞ Fit
(a)	$0.56Ro^{-1} + 0.73$
(b)	$2.17Ro^{-1} + 1.29$
(c)	$-3.43Ro^{-1} + 0.99$
(d)	$-0.01Ro^{-1} + 0.79$
(e)	$0.27Ro^{-1} + 0.81$
(f)	$-0.41Ro^{-1} + 1.11$
(g)	$4.04Ro^{-1} - 0.77$
(h)	$0.56Ro^{-1} + 1.09$

To isolate the Rossby dependence of torque, we normalize the magnitude of the measured torque, $G(Ro, Re)$ by $G_\infty(Re)$. As in *Paoletti and Lathrop* [2011] we plot G/G_∞ versus Ro^{-1} as it allows a piecewise linear model for the torque. For convenience in comparison to other work, empirical best fits to the data in Figures 3a–3h are given in Table 2.

The intersection of fit line (b) and fit line (c) are used to define the Rossby number where G/G_∞ peaks for $Ro < 0$. This is at $Ro^{-1} = -0.0547$ or $Ro = -18.3$.

The form of G/G_∞ has some interesting common features with that in Taylor-Couette (abbreviated TC) flow. Line (b) has the same slope as the analogous region in Taylor-Couette flow [*Paoletti and Lathrop*, 2011], and the peak $G/G_\infty \sim 1.2$ at the $Ro < 0$ peak is a similar enhancement above the torque with stationary outer boundary. The peak is in a different location: $Ro = -18.3$ instead of $Ro \sim -4$. However, *Brauckmann and Eckhardt* [2013] suggest that the location of this peak will shift substantially to higher *Ro* as radius ratio Γ is decreased in TC flow. It is plausible that similar behavior would be seen in spherical Couette.

It might seem surprising that the peak is not at $Ro^{-1} = 0$, but the fluid experiences a net rotation as the inner sphere spins even when the outer sphere is at rest. The situation that may best correspond to an effective absence of rotation is one in which the two spheres are counterrotating, the precise Rossby number depending on how the fluid is entrained by the two boundaries [*Dubrulle et al.*, 2005]. Since the fluid engagement with the inner sphere in our wide-gap configuration is less than that of the narrow-gap Taylor-Couette device of *Paoletti and Lathrop* [2011], it is not surprising that the peak is found at a much larger value of negative Rossby number here. It remains to explain why the torque is maximum in this particular place [*Brauckmann and Eckhardt*, 2013].

The form of G/G_∞ across zero inverse Rossby is also similar to that in TC flow. The intercept of Figure 3c must be unity by definition when the outer sphere is stationary, $Ro = \infty$ or $Ro^{-1} = 0$. The different slope for fit (c) is no surprise, since the slope is set by the peak location, peak size, and the $Ro = \infty$ intercept. Finally, we plot the "Rayleigh line" where the *equators* of the spheres have equal angular momentum:

$$Ro_R = \frac{1}{\Gamma^2} - 1 = +7.16 \tag{16}$$

or $Ro_R^{-1} = +0.14$. We note, as in Taylor-Couette flow, that G/G_∞ comes in with nearly zero slope approaching this line.

A full explanation of the Rossby dependence in Taylor-Couette flow is currently an area of active and ongoing research [*Ravelet et al.*, 2010; *Paoletti and Lathrop*, 2011; *van Gils et al.*, 2011; *Paoletti et al.*, 2012; *van Gils et al.*, 2012; *Huisman et al.*, 2012; *Brauckmann and Eckhardt*, 2013; *Ostilla et al.*, 2013] and may help to explain many features of Figure 3. However, we will note here a substantial difference from TC flow. In turbulent spherical Couette flow, G/G_∞ climbs substantially above $Ro^{-1} > 0.2$ and the flow undergoes several turbulent flow transitions at critical values of *Ro*. These transitions seem to reorganize the large-scale flow in a way that changes the angular momentum transport (and, as we will see, the internal magnetic field generation) substantially. The next section summarizes the dynamics in different ranges of *Ro*.

5. Large-Scale Flow Changes

5.1. Introduction

Our experiments and prior work have shown that the Rossby number *Ro* is a controlling parameter in selecting the large-scale turbulent flow pattern in hydrodynamic spherical Couette flow. Flows at different *Ro* can have different mean flows and large-scale fluctuations, and different states seem to have substantially different transport properties. It is important to note that these are likely *not* transitions between laminar/chaotic and fully turbulent states such as those that can be accessed at lower *Re*. As discussed in section 3.2, Reynolds number defined by the fluid's response to boundary forcing is typically well above 10^5 and strong broadband fluctuations are present in all measurements. At any fixed Rossby number, torque and other measurements scale as expected for a turbulent flow.

We would like to make a comment on the large asymmetry in the torque seen between positive and negative Ro^{-1} as its magnitude becomes large (nearing solid body rotation) in Figure 3. While the torque must be zero at solid body rotation, there is no particular reason to assume that G/G_∞ should take equal values on either side of solid body rotation. The inner sphere injects vorticity of opposing sign depending on the direction of rotation as viewed from the outer sphere rotating frame. At a given absolute value $|Ro^{-1}|$ we generally find very different behavior in all measured quantities for positive and negative values up until the point where we reach the RN and RP states described below, with the outer sphere rotating extremely slowly relative to the inner. Even then, the dynamics are similar but measurably different for positive and negative Rossby.

We have classified a number of flow regimes in Figure 3 and although boundaries between the states we have defined at different *Ro* are somewhat qualitative and precise boundaries in some transitions are not

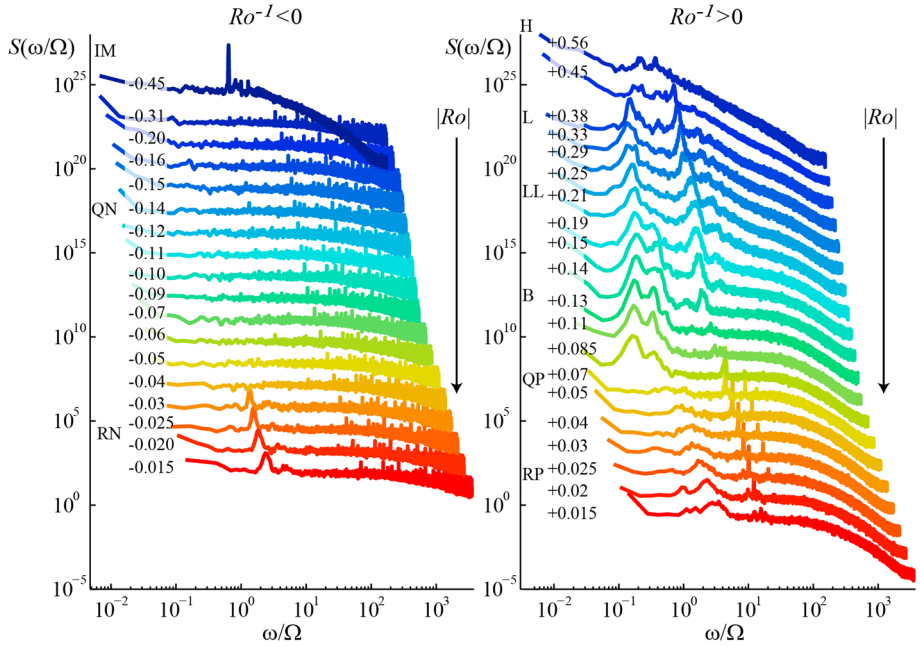

Figure 4. Wall shear stress frequency power spectra from water experiments showing the evolution of flow spectra with Ro^{-1}. The peaks in wall shear stress here are also observed as large wall pressure fluctuations (peak values approaching ρU^2 with $U = Ro\Omega_o(r_o - r_i)$) and in velocity measurements at several depths. This evidence suggests large-scale vortices. $Ro > 0$ state transitions involve measurable changes in angular momentum transport [*Zimmerman*, 2010; *Zimmerman et al.*, 2011]. We use spectral features to help define different turbulent flow states listed in the text. The flat spectra on the left are due to turbulent fluctuations, not instrument noise.The frequency response of constant temperature wall shear stress sensors depends on the mean flow, which may explain the different character of the high-frequency dependence in these spectra.

always clear, we want to summarize the differences in flow in different ranges of *Ro* appealing to the torque dependence in Figure 3 and flow power spectra in Figure 4 and describe the behavior in each.

5.2. Inertial Mode Dominated States: IM

Between solid body rotation and $Ro \sim -2.5$ (below $Ro^{-1} \sim -0.4$ in Figure 3) there are a sequence of different strong Coriolis-restored inertial modes along with substantial broadband turbulence. This process has been reported in *Kelley et al.* [2007, 2010], where the observed states were interpreted using full-sphere inertial modes as in *Zhang et al.* [2001]. Simulations were compared with experiments at $Ro = -0.6$ ($Ro^{-1} = -1.67$) in a magnetized system by *Matsui et al.* [2011]. The existence of equivalent modes in a spherical shell was addressed by calculations of nonaxisymmetric modes in our geometry in *Rieutord et al.* [2012], which also provides the details of observations of these inertial-mode dominated states in purely hydrodynamic flow in water. We refer the reader to the prior work for further discussion of these inertial mode states but include the wall shear stress power spectrum for $Ro^{-1} = 0.45$ ($Ro = -2.2$) in Figure 4 as a representative example.

We find here that transitions between inertial modes, while they occur in the runs we present here and represent a substantial restructuring of the overall large-scale flow, have little observed effect on angular momentum transport in Figure 3 or the internal field generation we describe in section 6.

5.3. Quiet States: QN and QP

For both negative and positive Rossby number, we find that there are turbulent states characterized by relatively quiet spectra, with broadband fluctuations but no strong spectral peaks, at least at low frequencies. The large spectral features in the EN, B, LL, and L states are associated with large globally correlated pressure fluctuations (with peak low pressures down to ρU^2 below ambient where $U = Ro\Omega_o(r_o - r_i)$) that seem to indicate systems of large-scale vortices like Rossby waves or inertial modes. The absence of these peaks in spectra is the most notable aspect of the quiet states QN ($-0.4 < Ro^{-1} < -0.033$) and QP, ($0.05 < Ro^{-1} < 0.067$).

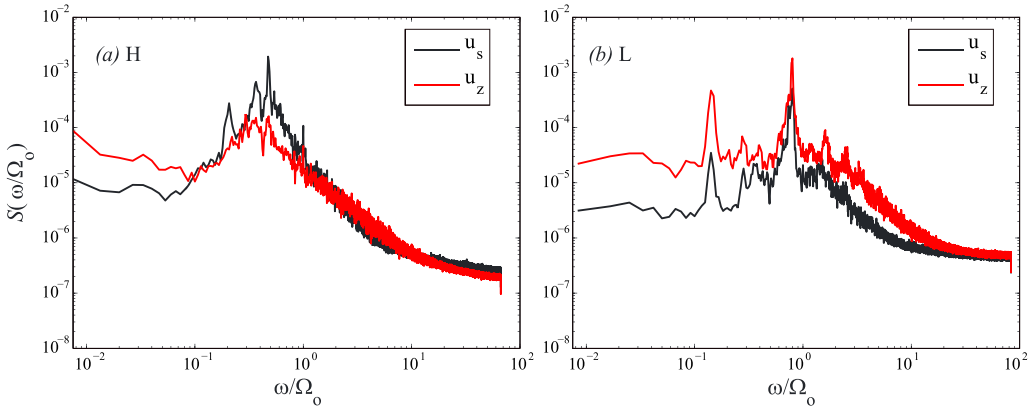

Figure 5. Power spectrum of cylindrical radial velocity u_s and vertical velocity u_z measured in (a) the high torque H state in water, $Ro = 1.7$, and (b) the low torque L state in water, $Ro = 2.7$. These spectra are measured well in the bulk flow, vertically down 50 cm from an instrumentation port on an intrusive stalk. The three peaks in the H spectrum are three drifting waves that are also observed in the magnetic induction at low field but are not strong in the wall shear stress. The weak peaks in the u_z spectrum for Figure 5a suggest that these waves have primarily horizontal velocities, as we might expect for Rossby waves.

5.4. Rotation Modified Outer Stationary: RN and RP

The turbulent flow in spherical Couette with the outer sphere stationary ($Ro^{-1} = 0$) and high enough Reynolds number (somewhere well above $Re = 10^5$) shows an energetic large-scale motion with azimuthal wave number $m = 1$ and a broad peak in the frequency spectrum centered on $\omega/\Omega_i = 0.04$ [*Zimmerman*, 2010]. The RN and RP states at high positive and negative Rossby ($|Ro^{-1}| < 0.03$) appear to be weakly modified versions of this outer stationary state encountered at infinite Rossby.

These states have a spectral signature in Figure 4 that narrows from a broad shallow bump in the spectrum to a fairly narrow peak as the system passes from positive to negative inverse Rossby through the outer stationary state. The frequency of the peak shifts with Ω_o, but this seems to be a Doppler shift of the $0.04\Omega_i$ frequency peak at different outer sphere rotation rates as the pressure sensors rotate around a flow in which the fluctuations have the same basic frequency.

5.5. High and Low Torque States and Transitions: H and L

The transition between the high torque H state and the low torque L state in Figures 3 and 4 has been characterized and analyzed in detail in *Zimmerman et al.* [2011].

Briefly, the higher torque H state in water is characterized by large azimuthal velocity and larger torque fluctuations and low azimuthal velocity measured at the instrumentation ports shown in Figure 1 [*Zimmerman et al.*, 2011]. The lower torque L state has faster azimuthal velocity at the port location, smaller fluctuations in azimuthal velocity and torque.

The torque dynamics are the same in the sodium. We refer the reader to *Zimmerman et al.* [2011] for complete details of these transitions, but the transition between a high azimuthal velocity low torque state and a low azimuthal velocity high torque state is important to understand the azimuthal magnetic field generation in section 6. We will see there that the H to L state transition is accompanied by a transition in the Ω effect.

In a transition region of *Ro* between the H and L states, the flow switches between the states as time goes on and the steep slope of line (g) in Figure 3 is primarily due to the changing residence time in each individual state as *Ro* is changed. G/G_∞ does vary with *Ro* within each state, but in the H-L transition, the dependence of the duty cycle on *Ro* dominates the steep variation observed in the region of Figure 3 fit line (g).

There is a pair of strong waves in the L state [*Zimmerman et al.*, 2011], seen clearly in frequency peaks in Figure 4 at $Ro = 2.6$ and $Ro = 3.0$ and in Figure 5b. The lower frequency wave with $\omega/\Omega_o = 0.18$ has azimuthal wave number $m = 1$, and the higher-frequency wave with frequency $\omega/\Omega_o = 0.25Ro + 0.16$ has $m = 2$. In the H state, however, the wall shear spectrum shown in Figure 4 and other measurements made at the location of the instrumentation ports all show fairly indistinct spectral features.

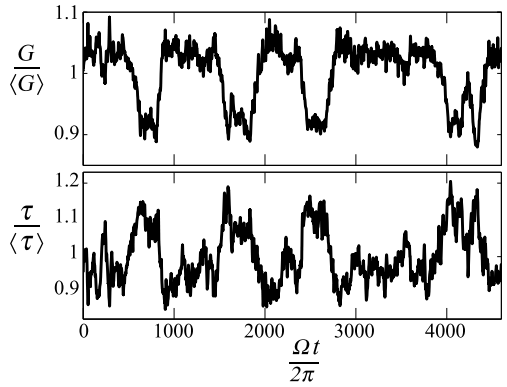

Figure 6. Time series of the L to LL state transitions in water at $Ro^{-1} = 0.31$. This is similar to the H to L turbulent bistability reported previously [*Zimmerman et al.*, 2011]. (top) The torque G and (bottom) the wall shear stress τ measured at an instrumentation port are both normalized by their long-term mean values. τ is low pass filtered with the same frequency cutoff as the torque to show the slow dynamics underlying the waves and the large broadband fluctuations.

However, measurements of magnetic induction in the weakly magnetized high torque state in sodium using the Hall sensor array show a drifting trio of globally correlated magnetic modes with $m = 1$, $m = 2$, and $m = 3$ with similar drift speed centered on $\omega/(m\Omega_o) = 0.2$. Peaks at these frequencies are also present in the H state in water in velocity measurements taken deeper inside the flow, shown in Figure 5a. In water, we measure cylindrical radial velocity, u_s, and vertical velocity u_z at a location 50 cm vertically down from an instrumentation port, well inside the bulk of the flow.

A frequency power spectrum of cylindrical radial velocity u_s at $Ro = 1.7$ is shown in Figure 5a. At this Ro, the $m = 1, 2, 3$ waves have frequencies $\omega/\Omega_o = 0.2, 0.37, 0.48$. The waves' drift is therefore somewhat desynchronized at this Ro, but as Ro is increased, the frequencies of the two higher waves change, and the waves become more closely synchronized in the intermittent state switching regime at $Ro = 2.1$.

We also plot the power spectrum of u_z in Figure 5a and note that the frequency peaks in the vertical velocity data are weak compared to the horizontal velocities, suggesting that the motions are nearly geostrophic, consistent with Rossby waves. The RMS level of the broadband velocity fluctuations outside the peaks is similar.

Figure 5b shows equivalent spectra at $Ro = 2.7$ in the low torque L state to highlight the difference in flow in the bulk. Here the two peaks evident in the wall shear stress spectra of Figure 4 in the L state are clearly present. These peaks are present in magnetic spectra, pressure spectra, wall shear stress spectra, and these deep velocity spectra. Unlike the H state spectra at this location, the vertical velocity fluctuations are larger at all frequencies, one substantial difference in the character of the turbulence seen here in the L state versus the H state.

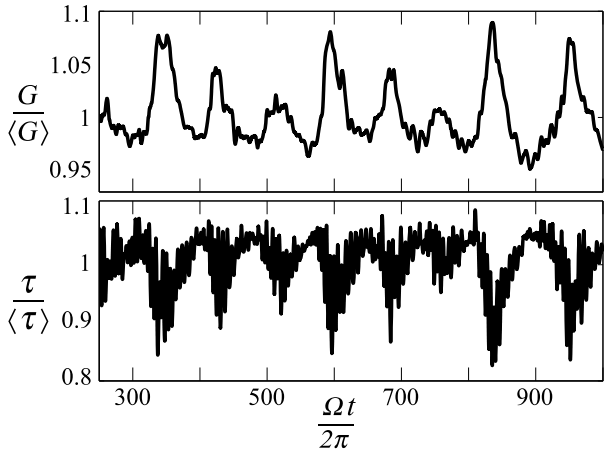

Figure 7. Time series of the B state in water at $Ro^{-1} = 0.16$. Bursts of higher torque occur on a background similar to the LL state. Torque G and wall shear stress τ are normalized by their mean values as in Figure 6. Again, the wall shear stress is low pass filtered like the torque.

5.6. States LL and B

The small jump in Figure 3 between the L and LL states appears to be a similar transition as that between the H and L states. Time series in the transition region between L and LL states are shown in Figure 6. We consider these jumps to be evidence of significant large-scale flow restructuring for two main reasons.

First, at lower and higher Ro than the narrow transition regions where we draw state boundaries, the RMS torque fluctuations on the inner sphere are substantially lower than those seen in Figure 6. Second, the largest fluctuations are slow (hundreds or thousands of sphere rotations) and show a clear correlation between the inner sphere and wall shear stress measurements on the outer sphere wall.

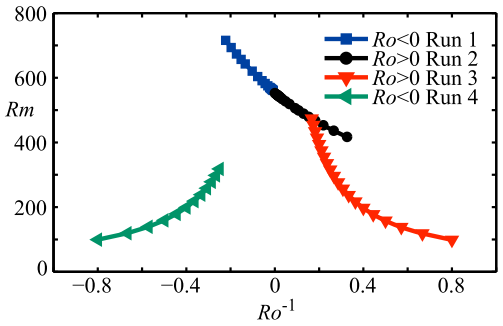

Figure 8. Parameter space map showing magnetic Reynolds number as a function of inverse Rossby number for the four runs of internal magnetic field measurements in Figure 9. All experiments are run at steady state, but there is a trend in *Rm* versus *Ro* because one sphere or the other is held at a fixed speed while the speed of the other is varied to change *Ro*.

The torque as a fraction of the long-term mean is shown on the top, and wall shear stress τ measured at a port as a fraction of the long-term mean is shown on the bottom. The lower torque LL state (existing for $0.2 < Ro^{-1} < 0.29$) is accompanied by a further increase of wall shear stress at the port radius.

The bursty state labeled B exists for $0.067 < Ro^{-1} < 0.2$. The transition from the LL to the B state shows another small drop in G/G_∞ around $Ro^{-1} = 0.2$. The torque shows peaked bursts toward a higher value in this state. A time series of torque and wall shear stress at $Ro^{-1} = 0.16$ is shown in Figure 7. Again, the torque variations on the inner sphere are correlated with lower wall shear stress at the ports on the outer sphere, suggesting that the bursts involve a large-scale phenomenon.

In the B state a third peak appears in the wall shear stress spectra in Figure 4, and as *Ro* is increased, eventually the higher-frequency peak from the LL state disappears. Throughout the B state, G/G_∞ varies little. At the transition from the B to the QP state, G/G_∞ begins to rise.

6. Magnetic Induction, Ω Effect

An important part of understanding the potential for a dynamo in turbulent spherical Couette flow is understanding the generation of internal fields. Here we examine the Ω effect by which azimuthal field is generated from poloidal field by differential rotation. We do this with weak applied magnetic field in this section, so that the Lorentz forces are relatively unimportant.

We measure internal azimuthal and cylindrical radial fields, B_ϕ and B_s, using a pair of Hall sensors located 60 cm from the axis of rotation and 10 cm outside the inner sphere's tangent cylinder (through one of the instrumentation ports in Figure 1e). The sensors are inside the end of a cylindrical stainless steel housing that is inserted parallel to the rotation axis so that the probe is submerged to a depth 10 cm from the wall of the outer sphere.

For several reasons, it was not practical to conduct the experiments in this paper with *Rm* or *Re* held constant with *Ro*. We understand the *Re* dependence of the torque in Figure 3 and data taken at different *Re* collapse onto one master curve of G/G_∞ versus *Ro*. We find that the induced field is not quite linear with *Rm* and do not have a better collapse at this time, so we present a parameter map of the steady state *Rm* at each value of Ro^{-1} in Figure 8.

The highest *Rm* achieved in any experiment here is 715 with strongly counterrotating boundaries. The generation of internal field will be stronger at higher *Rm*. The induction results in this section do not appear to scale exactly linearly in *Rm*, suggesting that flow modification from Lorentz force back reaction associated with the generation of these fields is already measurable, but this effect is fairly subtle. The internal fields in Figure 9 are measured over a large range of *Ro* with relatively weak applied magnetic field, $S = 0.39$ (20 A magnet current).

The fields from the internal probe are made dimensionless by B_{s0}, the predicted cylindrical radial component of the applied magnetic field at the location of the probe. As discussed previously, we use a calculated value from the magnet current that has been shown to agree with measurements with no flow so that it is easy to interpret the gain from mean induction. The choice to normalize by the cylindrical radial applied field B_{s0} is motivated by the assumption that mean azimuthal field generation at this location is caused by rotation-dominated shear flow with strong cylindrical radial dependence and weak axial dependence. If B_ϕ is generated predominately from B_s, then $B_\phi/B_{s0} > 1$ can be interpreted as Ω effect with gain.

The vertical component of the applied magnetic field, B_{z0}, at the internal probe's location is substantially stronger than the cylindrical component B_{s0}, with the ratio $B_{z0}/B_{s0} = 4.2$. If more of the observed B_ϕ is generated from B_z instead of B_s, then the gain due to the Ω effect is weaker but still present.

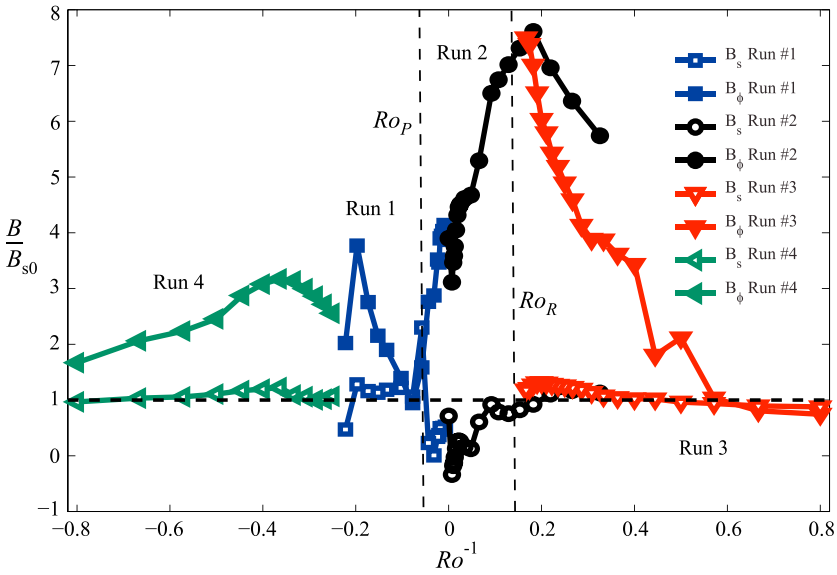

Figure 9. Mean cylindrical radial (B_s) and mean azimuthal (B_ϕ) field 10 cm down from the outer sphere surface at 60 cm cylindrical radius ($s = 0.4r_o$). We plot B_ϕ for $Ro > 0$ and $-B_\phi$ for $Ro < 0$ since its direction reverses as expected with negative differential rotation. B_{s0} is the cylindrical radial component of the externally applied field predicted at that location. In these data, the magnet current is 20 A, $S = 0.39$. Different experimental runs have different Rm, which is the main reason that, for example, the black "Run 2" and red "Run 3" curves do not coincide. Scaling by Rm almost collapses these, but not quite, evidence that the hydrodynamic base state is slightly modified by Lorentz force back reaction resulting from this internal field generation. However, there is little effect on the torque (Figure 3) or other measurements with this low applied field value, indicating similarity to the purely hydrodynamic flow.

6.1. Internal Field: Weak Applied Field

Figure 9 shows the internal azimuthal field, B_ϕ, and cylindrical radial, B_s, field as a function of Ro^{-1} at a fixed Lundquist number $S = 0.39$. When $Ro < 0$, we plot $-B_\phi$ because, as expected, B_ϕ reverses sign when the differential rotation does. It is useful to note here that the applied field has no ϕ component, so B_ϕ is entirely sourced by induction, but if there is no poloidal induction, we expect $B_s/B_{s0} = 1$. There is always measurable generation of B_ϕ in Figure 9.

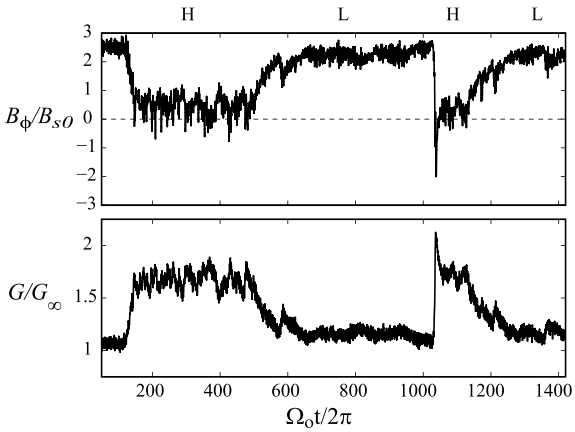

Figure 10. Time series of azimuthal field and torque at $Ro^{-1} = 0.47$, $Rm = 152$, $S = 0.59$ showing the importance of the hydrodynamic state on the Ω effect. At constant external driving parameters, the system undergoes intermittent transitions between the two states as described in *Zimmerman et al.* [2011] with very strong Ω effect in the low torque L state and weak and even occasionally reversed Ω effect in the high torque H state.

For comparison between Figures 9 and 3 we have also plotted the Rossby number of the $Ro < 0$ peak in G/G_∞ (Ro_P) and of the Rayleigh line, (Ro_R). The peak azimuthal field generation happens at about $Ro = 6$ or $Ro^{-1} = 0.167$ and shows large gain, up to a factor of 7.5 at $S = 0.39$, and a bit higher at lower S. The large jump around $Ro^{-1} = 0.5$ is the H-L transition. This is consistent with the picture in *Zimmerman et al.* [2011] of the emergence of a fast zonal flow with a sharp shear in the L state with a boundary near the tangent cylinder. The measurements in Figure 9 are taken at 1.2 times the tangent cylinder radius, and the strong Ω effect implies strong shear in the azimuthal velocity here.

In Figure 10 we show some transitions between high and low torque states at fixed Rossby $Ro^{-1} = 0.47$ with $S = 0.59$ and $Rm = 152$.

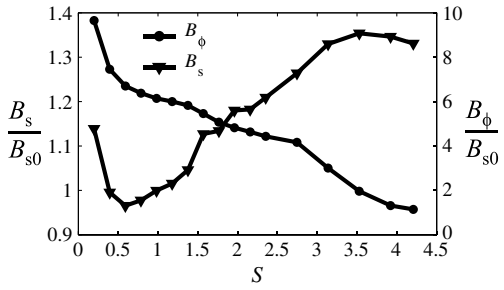

Figure 11. Azimuthal and cylindrical radial induced field at $Ro = 6$ (Bursty B hydrodynamic state) and $Rm = 477$ with varying Lundquist number S. B_ϕ (black circle) as a fraction of the applied field at the probe location is sharply reduced with increasing S, while B_s (black inverted triangle) grows appreciably.

At higher positive *Ro* than the H-L state transition, the Ω effect intensifies with increasing positive *Ro* up until the peak which is near the onset of the B state. The transition from the B to the QP state is accompanied by a drop in the Ω effect and a substantial increase in the mean poloidal induction. This induction is opposing the applied field, weakening and even reversing B_s.

The generation of B_ϕ at the probe location is greatly reduced near the negative Rossby peak in G/G_∞ (Ro_P in Figures 3 and 9), though the minimum Ω effect is slightly offset from the torque maximum. An interesting feature right at the G/G_∞ peak is strong poloidal induction aiding B_s, increasing it to more than twice the applied value.

This is reminiscent of the sharp peak of induced poloidal magnetic field reported by *Nataf et al.* [2008] in the DTS experiment. In that experiment, it was interpreted as a consequence of a stronger poloidal fluid flow as the geostrophic constraints due to rotation vanish.

There is substantial Ω effect for $Ro < 0$ as well, with a maximum value of $B_\phi/B_{s0} = 3.2$ at $Ro = -2.75$, $Ro^{-1} = -0.36$. Note, however, from Figure 8 that the magnetic Reynolds number here is about half that at the $Ro = 6$ peak and changes substantially with Ro^{-1} since in Run 4 we were keeping the outer sphere speed constant and changing $\Delta\Omega$. In fact, for $Ro^{-1} < -0.4$ the Ω effect scaled by *Rm* is about constant and about the same as that at the positive Rossby peak. We do expect strong shear near the tangent cylinder in this range, as in the simulations at $Ro^{-1} = -1.67$ by *Matsui et al.* [2011].

Predicting supercritical dynamo action in high Reynolds number spherical Couette flow requires the ability to capture the complex Rossby dependence of the flows and fields. Many of the Rossby-dependent features measured here have not been predicted or reported in spherical Couette simulations carried out at lower *Re*.

Some care should be taken with the Ω effect interpretation of Figure 9 since the measurements are taken at a single point. The strengthening and weakening of the azimuthal field in Figure 9 could reflect changes in the position of strong Ω effect toward or away from our measurement location rather than an increase or decrease in production of azimuthal field from poloidal field. Unfortunately, we cannot at this time move our probe significantly in cylindrical radius to test this idea. Still, the measurements of Figure 9 should be useful to compare against a similar point measurement taken from a simulation.

7. High Applied Field: Ω Effect Reduction and Dynamo-Like Bursts

The results in the preceding sections were in weak field regimes where the Lorentz force has little effect on the fluid flow. However, as the external magnetic field is increased, we access different states at given hydrodynamic parameters.

In this section we will describe results of increasing the applied field at $Ro = 6, E = 1.2 \times 10^{-7}$, and $Rm = 477$. This initial state is at the peak of the Ω effect for small Lundquist number in section 6.

7.1. Mean Internal Field: Strong Field

Figure 11 shows internal azimuthal and radial field induction (normalized by B_{s0}) as a function of Lundquist number. We may interpret B_ϕ/B_{s0} in Figure 11 as a reduction of the Ω effect due to growing Lorentz forces in the flow as the power required to produce the observed toroidal field substantially reduces the shear in the fluid. This is similar to a reduction of the Ω effect observed by *Verhille et al.* [2012].

Though B_ϕ/B_{s0} monotonically decreases throughout Figure 11, the strength of the azimuthal field B_ϕ increases up to $S = 2.75$, reaching a peak strength of 40 G. Above the kink in B_ϕ/B_{s0} at $S = 2.75$, B_ϕ drops and reaches a low of 17 G at the strongest applied field, $S = 4.2$.

As S is increased above 0.5, B_s/B_{s0} grows. This internal poloidal field growth is most likely concurrent with the observed increase of the mean external dipole moment described later, a phenomenon we believe

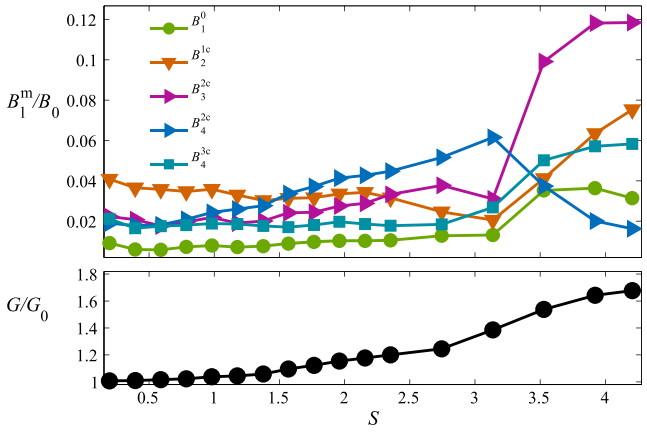

Figure 12. RMS fluctuations of $B_l^m = l(l+1)g_l^m$ for selected spherical harmonic contributions (top) normalized by the reference field B_0, and the torque on the inner sphere G (bottom) normalized by the torque at $S = 0$, G_0.

happens through a dynamo-style feedback loop involving both axisymmetric and nonaxisymmetric flow components.

7.2. Bursting State Onset

The drop in B_ϕ/B_{s0} as S is increased above 2.75 is shortly followed by the onset of a new flow state with much stronger fluctuations in several Gauss coefficients, significantly higher torque on the inner sphere, and bursts of the axial dipole Gauss coefficient g_1^0 in a direction that augments the applied field.

The onset of this dipole-bursting state is shown in Figure 12, which shows the RMS level of fluctuations ($B_l^m = l(l+1)g_l^m$) of each Gauss coefficient (or of a nonaxisymmetric pair representing an azimuthally drifting pattern). Above $S = 3.1$, there is a substantial increase in the strength of the nonaxisymmetric components B_2^1, B_3^2, and B_4^3, an increase in the fluctuations of B_1^0 and B_3^0, and an increase in the mean of B_1^0. Time series of these external field components at $S = 3.5$ are shown in Figure 13.

The torque on the inner sphere is also shown in Figure 12, normalized by its purely hydrodynamic value at zero applied field. The torque increases with S but begins to increase most rapidly around $S = 2.75$ where B_ϕ peaks, just before the growth of the strong fluctuations in the new state.

7.3. Mode Interactions: Time Evolution

In Figure 13 we show the time evolution of the state at $S = 3.5, Ro = 6, E = 1.2 \times 10^{-7}$, and $Rm = 477$. The quantity on top is $P_{sym} = P_1/\sigma_{P_1} + P_3/\sigma_{P_3}$ where P_1 and P_3 are the signals from two pressure sensors in

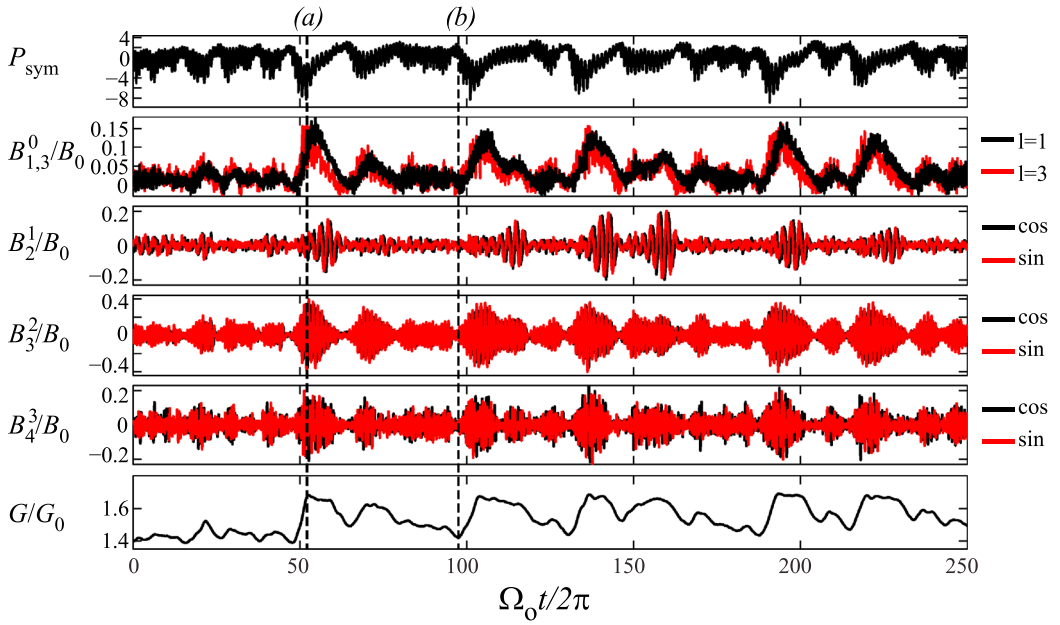

Figure 13. Time series at $S = 3.5$, near onset of the new dynamical state at strong S in Figure 12. $B_l^m = l(l+1)g_l^m$. In order from top, P_{sym}, sum of pressure signals from instrumentation port sensors located 180° apart, B_l^0, axisymmetric $m = 1$ and $m = 3$ magnetic field components, the most active nonaxisymmetric field components B_2^1, B_3^2, and B_4^3, and at the bottom, torque on the inner sphere normalized by the torque at $Ro = 6, S = 0$. These dynamics suggest dynamo-style feedback that enhances the applied field, as we discuss in the text.

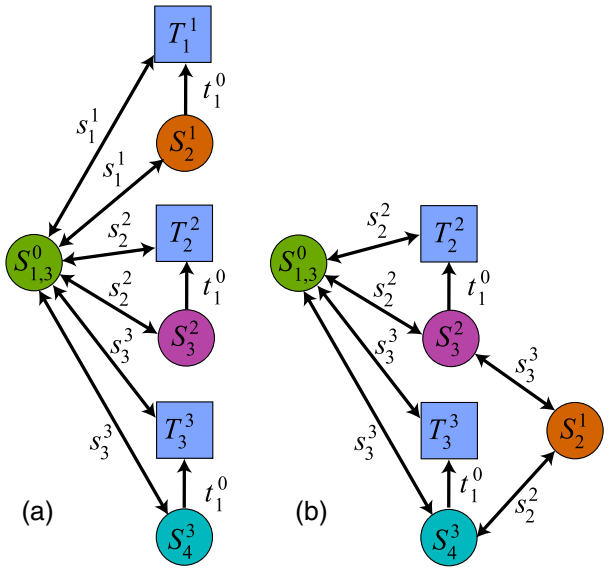

Figure 14. Two different interaction diagrams of externally measured magnetic field components S_l^m and internal field components T_l^m with underlying poloidal and toroidal velocity modes s_l^m and t_l^m are supported by our data. Directly observed external field components are in circles and colored as in Figure 12. We do not have spatial information about the internal toroidal fields, shown here in blue boxes. In scenario (a) the S_2^1 is induced from the axial dipole by a poloidal velocity field s_1^1. Instead, in (b) S_2^1 arises from the other two nonaxisymmetric modes, perhaps then causing a back reaction reducing the s_2^2 and s_3^3 velocity fields.

ports 180° apart, normalized by their standard deviations σ_{P_n} to remove slight differences in calibration. This combination emphasizes large-scale fluctuations with even azimuthal wave number m.

We plot five induced field components, the axisymmetric dipole B_1^0 and axisymmetric $l = 3$ component B_3^0. The contribution to these components from the applied field have been subtracted and positive values of B_1^0 correspond to an increase in the dipole that augments the applied field. The mean value of the dipole field B_1^0 averaged over many bursts is 5% above the applied value by $S = 4.2$. As discussed in section 2.3, the applied B_3^0 is opposite in sign to the applied B_1^0, and so the positive-going B_3^0 bursts in Figure 13 are reductions in the total B_3^0 field.

We also plot nonaxisymmetric components B_2^1, B_3^2, and B_4^3. The five poloidal components in Figure 13 dominate the fluctuations seen in the external measured field at these parameters. The nonaxisymmetric components rotate in a prograde direction with similar phase speeds, $\omega/(m\Omega_o) = 0.4$.

The growth of the nonaxisymmetric components B_3^2 and B_4^3 is clearly correlated with the growth of the axisymmetric components, and both are accompanied by increase in the torque on the inner sphere, shown at the bottom and normalized by its hydrodynamic value when $S = 0$. To guide the eye, lines (a) and (b) in Figure 13 are at a maximum and a minimum of the torque as a function of time.

The fluctuations in this section bear a resemblance to the behavior seen in the high torque state and the high-to-low transitions discussed in section 5. The high torque state at lower *Ro* and weak applied magnetic field discussed in section 5.5 also shows similar bursts of B_2^1, B_3^2, and B_4^3 synchronized with mean and fluctuating enhancements of the dipole. Many of the details of the temporal dynamics are different, though. The trio of nonaxisymmetric components drift half as fast at $Ro \simeq 2$ than $Ro = 6$. The weakly magnetized high torque state also shows mean and fluctuating dipole enhancement synchronized with the growth of the nonaxisymmetric modes.

7.4. A Possible Dynamo-Style Feedback

The coupling between the nonaxisymmetric components and the axisymmetric components in Figure 13 is notable. Using the selection rules for flow and field from *Bullard and Gellman* [1954], we can put forth two conjectures on the nature of the dipole-reinforcing bursts. Here we will use s_l^m and t_l^m for poloidal and toroidal *velocity* components and S_l^m and T_l^m for poloidal and toroidal *magnetic field* components. There can be no toroidal field in the current-free region external to the sphere, so all of the components we directly observe are external poloidal fields S_l^m. We note that whenever a magnetic field is induced by a velocity field, energy and momentum conservation require a Lorentz force effect on the velocity field. The enhanced torque in this state is also evidence of significant Lorentz forces.

We assume underlying nonaxisymmetric flow components with $m = 1$, $m = 2$, and $m = 3$. P_{sym} in Figure 13 is direct evidence for a $m = 2$ flow component synchronized with the S_3^2 external induction.

Our imposed differential rotation is expected to be dominated by the axisymmetric component t_1^0. This t_1^0 flow could lead to substantial gain in magnetic field, though that gain is reduced from the hydrodynamic base state as per Figure 11.

Each burst of B_1^0 and B_3^0 in Figure 13 is synchronized with the growth of the nonaxisymmetric components B_3^2 and B_4^3. *Spence et al.* [2006] were the first to report on the induction of an axisymmetric dipole in the Madison dynamo experiment. They demonstrate that an axial dipole moment measured external to the current-carrying region cannot be induced directly from an axisymmetric applied field by an axisymmetric flow. *Spence et al.* [2006] explain their external axial dipole induction as the net contribution of the nonaxisymmetric turbulent fluctuations.

We note that the induced dipole adds to the imposed field in our case, while in the Madison experiment it was always opposite, reducing the total dipole.

We show several possibilities of allowed interactions in Figure 14a, assuming that the internal nonaxisymmetric components are the poloidal flows s_1^1, s_2^2, and s_3^3. There is a one-step coupling by which those velocity fields can induce the observed nonaxisymmetric fields from the applied axisymmetric field. We do not draw an exhaustive network diagram in Figure 14a, as there are 41 allowed interactions involving just the eight field components and four flow components shown there, just to list a few simple possibilities that are consistent with the behavior in Figure 13.

There are three conceptually similar triads (e.g., S_1^0, S_3^2, and T_2^2) where an underlying s_l^l velocity component induces the externally observed poloidal component S_{l+1}^l from S_1^0 and S_3^0. That poloidal component is converted to an internal toroidal T_l^l by the action of the differential rotation t_1^0, and the T_l^l toroidal component can be converted to S_1^0 and S_3^0 by the s_l^l poloidal velocity field. Note that each triad has a possible dynamo mechanism similar to that discussed in *Bullard and Gellman* [1954].

We present another similar interaction diagram in Figure 14b, this time inducing the S_2^1 component from either of the large S_3^2 or S_4^3 fields. Note that in Figure 13 S_2^1 arises slightly later than either S_3^2 or S_4^3. Also evident is that as S_2^1 grows, the enhanced dipole S_1^0 and modes S_3^2 and S_4^3 fall, possible evidence for a strong Lorentz force back reaction caused by the production of S_2^1. Again, we do not show the large number of total possible connections.

Assuming some radial dependence for the internal flow and field components and constructing a reduced induction equation model could be fruitful, as it would allow us to know which interactions were strongest, but this is beyond the scope of this paper. Nevertheless, these are more results that could provide a good benchmark for geodynamo codes.

As we do not have conclusive evidence supporting either scenario in Figure 14, we have included both for scientific completeness. We expect future research can distinguish between them. A complete understanding of the scenarios set out in Figure 14 may be of particular geophysical relevance. The observations here are consistent with differential rotation generating toroidal field plus a few nonaxisymmetric drifting components that may be similar to Rossby waves. In this sense, they would be similar to the cartridge belt dynamo scenario seen in the onset of rotating convection in a spherical shell.

The fact that we seem to have *large-scale* poloidal motions closing an axial-dipole-enhancing induction loop is encouraging. It points to the possibility of understanding these dynamics with reduced models of the flow and untangling how the small-scale turbulence interacts with the large-scale motions in both magnetized and unmagnetized states.

8. Summary and Conclusions

We present a number of novel experimental results in hydrodynamic and hydromagnetic spherical Couette experiments at unprecedented magnetic and hydrodynamic Reynolds number. We look at angular momentum transport without appreciable magnetic field effects and find broad similarity with recent results from Taylor-Couette flow over part of the accessible range of Rossby number but find dramatic restructuring of the flow and strong enhancement of angular momentum transport, possibly involving large-scale Rossby waves, when $1 < Ro < 5$. Changing *Re* alone while holding *Ro* fixed leads to expected turbulent flow scalings. The similarities and differences in the *Ro* dependence of turbulent angular momentum transport between spherical and Taylor Couette flow may have interesting implications for understanding angular momentum transport in rotating geophysical systems.

The *Ro* dependence of the hydrodynamic mean flow confers a strong Rossby dependence on the Ω effect, the generation of internal azimuthal magnetic field from poloidal field. Although we do not observe a

self-excited magnetic dynamo in the current set of experiments up to half speed, we do observe substantial gain in the poloidal-to-toroidal field conversion over a large range of *Ro*.

Applying a strong magnetic field at $Ro = 6$, the peak of low-field azimuthal field generation, reduces the Ω effect, a phenomenon that may be important for saturation of geophysical and astrophysical dynamos. Strong enough field leads to the onset of a different dynamical state with higher torque and bursts of non-axisymmetric magnetic field and velocity fluctuations that are correlated with bursts in enhancement of axisymmetric external fields. The nonaxisymmetric fluctuations, like those in the high torque hydrodynamic state, seem to be a trio of drifting waves that may be Rossby waves.

The dipole bursts are plausibly generated by a dynamo-style feedback loop that involves differential rotation and drifting waves, a scenario that is of substantial geophysical and astrophysical interest. We are just at the beginning of hydromagnetic experiments in this facility, but these early results suggest a rich interplay of turbulence, rotation, and magnetic fields, as in a planet's liquid metal core.

Acknowledgments
We gratefully acknowledge grant support from NSF Earth Sciences. Design and construction of this major research facility were supported by NSF/MRI EAR-0116129, and continuing scientific work is supported by NSF EAR-1114303. We thank Don Martin and Nolan Ballew at UMD for invaluable technical support and Simon Cabanes from UJF Grenoble for help with the Hall sensor array design and installation, and Matthew Adams at UMD for help with experimental runs. The stay of H.C.N. at UMD was made possible, thanks to support by UMD, CNRS, and University of Grenoble under Memorandun of Understanding CNRS-723684/00.

References

Berhanu, M., et al. (2007), Magnetic field reversals in an experimental turbulent dynamo, *Europhys. Lett.*, *77*(5), 59,001, doi:10.1209/0295-5075/77/59001.

Berhanu, M., et al. (2010), Dynamo regimes and transitions in the VKS experiment, *Eur. Phys. J. B*, *77*(4), 459–468, doi:10.1140/epjb/e2010-00272-5.

Brauckmann, H. J., and B. Eckhardt (2013), Intermittent boundary layers and torque maxima in Taylor-Couette flow, *Phys. Rev. E*, *87*, 033004, doi:10.1103/PhysRevE.87.033004.

Brito, D., T. Alboussière, P. Cardin, N. Gagnière, D. Jault, P. La Rizza, J.-P. Masson, H.-C. Nataf, and D. Schmitt (2011), Zonal shear and super-rotation in a magnetized spherical Couette-flow experiment, *Phys. Rev. E*, *83*(6), 066310, doi:10.1103/PhysRevE.83.066310.

Bullard, E., and H. Gellman (1954), Homogeneous dynamos and terrestrial magnetism, *Philos. Trans. R. Soc. London, Ser. A*, *247*(928), 213–278.

Busse, F. H. (1970), Thermal instabilities in rapidly rotating systems, *J. Fluid Mech.*, *44*(3), 441–460.

Cardin, P., D. Brito, D. Jault, H.-C. Nataf, and J.-P. Masson (2002), Towards a rapidly rotating liquid sodium dynamo experiment, *Magnetohydrodynamics*, *38*(1), 177–189.

Dubrulle, B., O. Dauchot, F. Daviaud, P.-Y. Longaretti, D. Richard, and J.-P. Zahn (2005), Stability and turbulent transport in Taylor–Couette flow from analysis of experimental data, *Phys. Fluids*, *17*(9), 095103, doi:10.1063/1.2008999.

Fink, J., and L. Leibowitz (1995), Thermodynamic and transport properties of sodium liquid and vapor, *Tech. Rep. ANL/RE–95/2*, Argonne National Laboratory.

Frick, P., V. Noskov, S. Denisov, and R. Stepanov (2010), Direct measurement of effective magnetic diffusivity in turbulent flow of liquid sodium, *Phys. Rev. Lett.*, *105*(18), 184502, doi:10.1103/PhysRevLett.105.184502.

Gailitis, A., O. Lielausis, E. Platacis, S. Dement'ev, A. Cifersons, G. Gerbeth, T. Gundrum, F. Stefani, M. Christen, and G. Will (2001), Magnetic field saturation in the Riga dynamo experiment, *Phys. Rev. Lett.*, *86*, 3024–3027, doi:10.1103/PhysRevLett.86.3024.

Gailitis, A., G. Gerbeth, T. Gundrum, O. Lielausis, E. Platacis, and F. Stefani (2008), History and results of the Riga dynamo experiments, *C.R. Phys.*, *9*(7), 721–728, doi:10.1016/j.crhy.2008.07.004.

Gillet, N., D. Jault, E. Canet, and A. Fournier (2010), Fast torsional waves and strong magnetic field within the Earth's core, *Nature*, *465*(7294), 74–77, doi:10.1038/nature09010.

Gillet, N., N. Schaeffer, and D. Jault (2011), Rationale and geophysical evidence for quasi-geostrophic rapid dynamics within the Earth's outer core, *Phys. Earth Planet. Inter.*, *187*(3–4), 380–390, doi:10.1016/j.pepi.2012.03.006.

Holme, R. (2007), Large-scale flow in the core, in *Treatise on Geophysics*, vol. 8, Core Dynamics, edited by P. Olson and G. Schubert, pp. 107–129, Elsevier B. V., Amsterdam.

Huisman, S. G., D. P. M. van Gils, S. Grossmann, C. Sun, and D. Lohse (2012), Ultimate turbulent Taylor-Couette flow, *Phys. Rev. Lett.*, *108*(024,501), doi:10.1103/PhysRevLett.108.024501.

Jackson, D. (1975), *Classical Electrodynamics*, John Wiley, New York.

Jault, D. (2008), Axial invariance of rapidly varying diffusionless motions in the Earth's core interior, *Phys. Earth Planet. Inter.*, *166*, 67–76.

Kelley, D. H., S. A. Triana, D. S. Zimmerman, A. Tilgner, and D. P. Lathrop (2007), Inertial waves driven by differential rotation in a planetary geometry, *Geophys. Astrophys. Fluid Dyn.*, *101*(5–6), 469–487, doi:10.1080/03091920701561907.

Kelley, D. H., S. A. Triana, D. S. Zimmerman, and D. P. Lathrop (2010), Selection of inertial modes in spherical Couette flow, *Phys. Rev. E*, *81*(2), 026311, doi:10.1103/PhysRevE.81.026311.

Lathrop, D., W. Shew, and D. Sisan (2001), Laboratory experiments on the transition to MHD dynamos, *Plasma Phys. Controlled Fusion*, *43*(12A), A151–A160, doi:10.1088/0741-3335/43/12A/311, 28th EPS Conference on Controlled Fusion and Plasma Physics, FUNCHAL, PORTUGAL, JUN 18-22, 2001.

Lemmon, E., M. McLinden, and D. Friend (2013), *NIST Chemistry WebBook*. NIST Standard Reference Database Number 69, chap., Thermophysical Properties of Fluid Systems, National Institute of Standards and Technology, Gaithersburg, Md.

Matsui, H., M. Adams, D. Kelley, S. Triana, D. Zimmerman, B. Buffet, and D. Lathrop (2011), Numerical and experimental investigation of shear-driven inertial oscillations in an Earth-like geometry, *Phys. Earth Planet. Inter.*, *188*, 194–202, doi:10.1016/j.pepi.2011.07.012.

Monchaux, R., et al. (2007), Generation of a magnetic field by dynamo action in a turbulent flow of liquid sodium, *Phys. Rev. Lett.*, *98*(4), 044502, doi:10.1103/PhysRevLett.98.044502.

Monchaux, R., et al. (2009), The von Kármán Sodium experiment: Turbulent dynamical dynamos, *Phys. Fluids*, *21*(3), 035108, doi:10.1063/1.3085724.

Nataf, H.-C. (2013), Magnetic induction maps in a magnetized spherical Couette flow experiment, *C.R. Phys.*, *14*(2–3), 248–267, doi:10.1016/j.crhy.2012.12.002.

Nataf, H.-C., and N. Gagnière (2008), On the peculiar nature of turbulence in planetary dynamos, *C.R. Phys.*, *9*(7), 702–710, doi:10.1016/j.crhy.2008.07.009.

Nataf, H.-C., T. Alboussière, D. Brito, P. Cardin, N. Gagnière, D. Jault, and D. Schmitt (2008), Rapidly rotating spherical Couette flow in a dipolar magnetic field: An experimental study of the mean axisymmetric flow, *Phys. Earth Planet. Inter.*, *170*, 60–72, doi:10.1016/j.pepi.2008.07.034.

Ostilla, R., R. J. A. M. Stevens, S. Grossmann, R. Verzicco, and D. Lohse (2013), Optimal Taylor Couette flow: Direct numerical simulations, *J. Fluid Mech*, *719*, 14–46, doi:10.1017/jfm.2012.596.

Paoletti, M. S., and D. P. Lathrop (2011), Angular momentum transport in turbulent flow between independently rotating cylinders, *Phys. Rev. Lett.*, *106*(2), 024501, doi:10.1103/PhysRevLett.106.024501.

Paoletti, M. S., D. P. M. van Gils, B. Dubrulle, C. Sun, D. Lohse, and D. P. Lathrop (2012), Angular momentum transport and turbulence in laboratory models of Keplerian flows, *A&A*, *547*, A64, doi:10.1051/0004-6361/201118511.

Petrelis, F., M. Bourgoin, L. Marie, J. Burguete, A. Chiffaudel, F. Daviaud, S. Fauve, P. Odier, and J. Pinton (2003), Nonlinear magnetic induction by helical motion in a liquid sodium turbulent flow, *Phys. Rev. Lett.*, *90*(17), 174501, doi:10.1103/PhysRevLett.90.174501.

Rahbarnia, K., et al. (2012), Direct observation of the turbulent EMF and transport of magnetic field in a liquid sodium experiment, *Astrophys. J.*, *759*(2), 80.

Ravelet, F., R. Delfos, and J. Westerweel (2010), Influence of global rotation and reynolds number on the large-scale features of a turbulent Taylor-Couette flow, *Phys. Fluids*, *22*(5), 055103, doi:10.1063/1.3392773.

Rieutord, M., S. Triana, D. Zimmerman, and D. Lathrop (2012), Excitation of inertial modes in an experimental spherical Couette flow, *Phys. Rev. E*, *86*, 026304, doi:10.1103/PhysRevE.86.026304.

Sisan, D. R. (2004), Hydromagnetic turbulent instability in liquid sodium experiments, PhD thesis, University of Maryland, College Park, Md.

Spence, E. J., M. D. Nornberg, C. M. Jacobson, R. D. Kendrick, and C. B. Forest (2006), Observation of a turbulence-induced large scale magnetic field, *Phys. Rev. Lett.*, *96*, 055002, doi:10.1103/PhysRevLett.96.055002.

Stieglitz, R., and U. Müller (2001), Experimental demonstration of a homogeneous two-scale dynamo, *Phys. Fluids*, *13*, 561–564, doi:10.1063/1.1331315.

van Gils, D. P. M., S. G. Huisman, G.-W. Bruggert, C. Sun, and D. Lohse (2011), Torque scaling in turbulent Taylor-Couette flow with co- and counterrotating cylinders, *Phys. Rev. Lett.*, *106*(2), 024502, doi:10.1103/PhysRevLett.106.024502.

van Gils, D. P. M., S. G. Huisman, S. Grossmann, C. Sun, and D. Lohse (2012), Optimal Taylor-Couette turbulence, *J. Fluid Mech.*, *706*, 118–149, doi:10.1017/jfm.2012.236.

Verhille, G., R. Khalilov, N. Plihon, P. Frick, and J.-F. Pinton (2012), Transition from hydrodynamic turbulence to magnetohydrodynamic turbulence in von Kármán flows, *J. Fluid Mech.*, *693*, 243–260, doi:10.1017/jfm.2011.522.

Wicht, J. (2014), Flow instabilities in the wide-gap spherical couette system, *J. Fluid Mech.*, *738*, 184–221, doi:10.1017/jfm.2013.545.

Zhang, K., P. Earnshaw, X. Liao, and F. H. Busse (2001), On inertial waves in a rotating fluid sphere, *J. Fluid Mech.*, *437*, 103–119, doi:10.1017/S0022112001004049.

Zimmerman, D. S. (2010), Turbulent shear flow in a rapidly rotating spherical annulus, PhD thesis, University of Maryland, College Park, Md.

Zimmerman, D. S., S. A. Triana, and D. P. Lathrop (2011), Bi-stability in turbulent, rotating spherical Couette flow, *Phys. Fluids*, *23*(6), 065104, doi:10.1063/1.3593465.